AGU PUBLICATIONS

JGR

Journal of Geophysical Research: Oceans

RESEARCH ARTICLE

10.1002/2015JC011254

Key Points:
- Observations and modeling of albedo and transmittance of thin (<15 cm) sea ice
- High brine volumes impact the spectral optical properties

Correspondence to:
T. Taskjelle,
torbjorn.taskjelle@uib.no

Citation:
Taskjelle, T., S. R. Hudson, M. A. Granskog, M. Nicolaus, R. Lei, S. Gerland, J. J. Stamnes, and B. Hamre (2016), Spectral albedo and transmittance of thin young Arctic sea ice, *J. Geophys. Res. Oceans*, *121*, 540–553, doi:10.1002/2015JC011254.

Received 19 AUG 2015
Accepted 11 DEC 2015
Accepted article online 18 DEC 2015
Published online 14 JAN 2016

Spectral albedo and transmittance of thin young Arctic sea ice

Torbjørn Taskjelle[1], Stephen R. Hudson[2], Mats A. Granskog[2], Marcel Nicolaus[3], Ruibo Lei[4], Sebastian Gerland[2], Jakob J. Stamnes[1], and Børge Hamre[1]

[1]Department of Physics and Technology, University of Bergen, Bergen, Norway, [2]Norwegian Polar Institute, Fram Centre, Tromsø, Norway, [3]Alfred-Wegener-Institut, Helmholtz-Zentrum für Polar- und Meeresforschung, Bremerhaven, Germany, [4]SOA Key Laboratory for Polar Science, Polar Research Institute of China, Shanghai, China

Abstract Spectral albedo and transmittance in the range 400–900 nm were measured on three separate dates on less than 15 cm thick new Arctic sea ice growing on Kongsfjorden, Svalbard at 78.9°N, 11.9°E. Inherent optical properties, including absorption coefficients of particulate and dissolved material, were obtained from ice samples and fed into a radiative transfer model, which was used to analyze spectral albedo and transmittance and to study the influence of clouds and snow on these. Integrated albedo and transmittance for photosynthetically active radiation (400–900 nm) were in the range 0.17–0.21 and 0.77–0.86, respectively. The average albedo and transmittance of the total solar radiation energy were 0.16 and 0.51, respectively. Values inferred from the model indicate that the ice contained possibly up to 40% brine and only 0.6% bubbles. Angular redistribution of solar radiation by clouds and snow was found to influence both the wavelength-integrated value and the spectral shape of albedo and transmittance. In particular, local peaks and depressions in the spectral albedo and spectral transmittance were found for wavelengths within atmospheric absorption bands. Simulated and measured transmittance spectra were within 5% for most of the wavelength range, but deviated up to 25% in the vicinity of 800 nm, indicating the need for more optical laboratory measurements of pure ice, or improved modeling of brine optical properties in this near-infrared wavelength region.

1. Introduction

Due to the high albedo of sea ice compared to open water, sea ice acts as a radiation shield that greatly reduces the solar energy entering the Arctic Ocean, thus limiting biological activity and ocean heating [e.g., *Arrigo et al*., 2008; *Perovich*, 1996]. But the sea ice cover is not a solid, continuous area of ice. It breaks up due to forcing by wind or currents to form leads, which are important for the exchange of heat and radiative energy between atmosphere and ocean [e.g., *Eisen and Kottmeier*, 2000]. During the first half of the sunlit season, air temperatures are low enough to permit new ice to form in leads. Further, during early stages of autumn freezeup there may be large areas of new, thin ice while the sun is still above the horizon [*Ehn et al*., 2007]. Such thin ice allows more light to enter the ocean than thicker ice or snow-covered ice, but less than open water. Understanding the radiative properties of thin ice is therefore necessary and important in order to gain a complete understanding of the light conditions in the Arctic Ocean.

Ice thicker than 1 m keeps much of the incident sunlight from reaching the ocean, especially when snow covered. *Nicolaus et al*. [2010] reported mean PAR (photosynthetically active radiation) transmittances in the range 0.001–0.097 for about 2 m thick ice during the Tara Drift of 2007, the highest values occurring after all snow had melted. *Light et al*. [2015] reported peak transmittances of 0.05–0.3 in the 380–890 nm region for 0.83–2.04 m thick bare, melting ice, during the ICESCAPE cruise. *Ehn et al*. [2011] found PAR transmittance of 0.05–0.16 through 0.66–1.25 m thick bare ice. *Ehn et al*. and Light et al. measured transmittance through both melt ponds and bare ice, with higher transmittances seen for the ponded areas, partly due to thinner ice below ponds.

Many studies have concentrated on thick ice [e.g., *Light et al*., 2008; *Frey et al*., 2011; *Nicolaus et al*., 2013; *Hudson et al*., 2013] in addition to the studies mentioned above. A few studies have focused on thin ice, including *Grenfell* [1979], who used a radiative transfer model with optical properties of sea ice from *Grenfell*

and Maykut [1977], to investigate the effect of ice thickness (in the range 0.2–0.8 m) on albedo and transmittance. *Perovich and Grenfell* [1981] reported on the optical properties of ice up to 25 cm thick, which was grown in a laboratory. *Perovich* [1991] measured albedo in a freezing lead during autumn and used a radiative transfer model to estimate transmittance, in the 400–1000 nm range. For 10 cm thick ice, he obtained bulk values of 0.14 and 0.80 for albedo and transmittance, respectively. The transmittance dropped to 0.47 for 13 cm thick ice with 0.5 cm snow cover. The snow caused an increase of albedo to 0.48. *Ishikawa et al.* [2002] cut holes in existing ice and performed measurements on the new ice forming in the artificial lead. They measured albedo and transmittance for wavelengths in the range 400–1050 nm, as well as heat fluxes, as the ice grew from 0 to 11 cm. They found transmittances of 0.42 and higher for snow-free ice near Finland, and around 0.2 and higher for snow-covered ice near Japan. *Rasmus et al.* [2002] performed measurements of albedo and transmittance on about 30 cm thick ice in the Gulf of Finland, for wavelengths in the range 300–850 nm. The PAR transmittance was reported to be 0.136. In these studies, measurements were not performed of the absorption by particles and CDOM (chromophoric dissolved organic matter) in the ice. A more comprehensive study in the same region as that by *Rasmus et al.* [2002] is that by *Ehn et al.* [2004]. Ehn et al. found spectral transmittance between 0.25 and 0.42 in the PAR region for most of the measuring period, with ice thicknesses of 21–28 cm. After the ice had melted to a thickness of 10 cm, spectral transmittance was seen to be 0.66–0.73 in the PAR region.

Here we present measurements of albedo and transmittance spectra performed on newly formed ice in Kongsfjorden, near Ny-Ålesund, Svalbard, as well as results of analyses of measured spectra using a radiative transfer model to which measured CDOM and particle absorption are parts of the input. Several previous studies of the optical properties of sea ice have been performed in Kongsfjorden [*Gerland et al.*, 1999; *Hamre et al.*, 2004] though not on ice this thin.

One of the motivations for this work is the rather few studies on very thin ice at high latitudes. With the ice cover becoming thinner and younger [*Maslanik et al.*, 2007], we are seeing a more seasonal ice cover in the Arctic [*Zhang and Walsh*, 2006]. A thinner ice cover may be more fragile and dynamic, and therefore see more refreezing leads, and hence more new ice. These ongoing changes in the Arctic sea ice cover make knowledge about new, thin ice important for a more complete understanding of radiative processes in the ice-covered Arctic.

2. Measurements and Modeling

2.1. Measurements

Measurements of albedo and transmittance of growing sea ice were made in April 2010, near Ny-Ålesund, Svalbard, as part of the project AMORA (Advancing Modeling and Observing solar Radiation of Arctic sea-ice) [*Nicolaus et al.*, 2015] and monitoring of sea ice in Kongsfjorden [*Gerland and Renner*, 2007]. The ice started forming on 15 April, and data were collected 17, 21, and 25 April. During this 9 day period the ice grew from a thickness of 7–14.6 cm. The ice was free from snow the two first days, while on 25 April a layer of fresh slushy snow with a thickness of about 2 mm had fallen on the ice. This snow layer melted gradually during the measurement period. The albedo and transmittance measurements were repeated after removing the remaining snow along the transmittance transect, but leaving the snow untouched under the stationary rack for albedo measurements. On all 3 days the ice along the measurement transects appeared homogeneous by eye.

Irradiances above and below the ice were measured using three Ramses ACC-VIS hyperspectral irradiance sensors (TriOS Mess- und Datentechnik GmbH, Rastede, Germany). These are cosine collectors with a wavelength range of 320–950 nm. Above the ice, two sensors were mounted on a rack about 1 m above the surface, measuring the downward and upward irradiance. Below the ice, a sensor mounted on a sled made of light blue expanded polystyrene, similar to that used by *Nicolaus et al.* [2013], measured the downward irradiance. The sled was pushed 10–15 m away from an entrance hole cut in the ice, pulled back in steps of about 0.5 m, and the downward irradiance was measured at each step. Irradiance spectra under ice free from snow were obtained at 42 and 21 points along the transect on 17 and 21 April, respectively. On 25 April, irradiance spectra were obtained, first at 14 positions under the snow-covered ice, and then at 11 positions after removal of the snow. The entrance hole for the sled was a few meters away from the albedo rack (Figure 1). The sensor underneath the ice was placed about 1 cm from the ice bottom (see inset of Figure 1), where the sled is

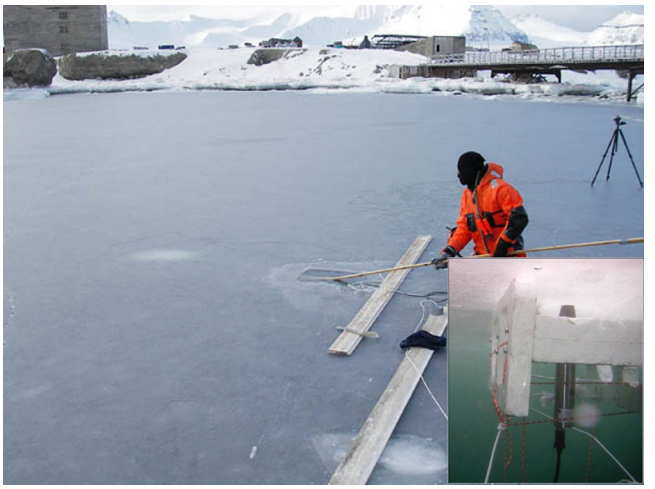

Figure 1. Photo showing irradiance measurements. The sled (see inset) below the ice is seen through the ice as a white spot to the left of the entrance hole. The tripod seen to the right is part of the rack holding the two sensors measuring upward and downward irradiance above the ice.

shown. Data from the under-ice sensor were calibrated using the manufacturer's immersion-corrected calibration coefficients, which account for the change in the cosine collector's efficiency when submerged in water. Figure 1 also shows that the sled is visible through the ice. It is seen as a white patch just to the left of the entrance hole.

Although the sensors operated in the range 320–950 nm, we consider measured irradiances only in the range 400–900 nm here, since comparisons between different sensors show unsatisfactory agreement outside this wavelength range. Due to lacking intercalibration, a correction was applied to the albedo and transmittance values, determined by placing the two corresponding sensors next to each other pointing in the same direction, and calculating the ratio of the measured irradiances. Albedo and transmittance was then divided by the irradiance ratio for the respective pair of sensors, giving corrections of no more than 2.6% at any wavelength.

The cloud cover varied during the field campaign. On 17 April the sky was clear, on 21 April there was a thin high cloud layer through which the sun was visible, as well as low stratus clouds in the surrounding sky, and on 25 April there were some scattered clouds, mostly not covering the sun.

Since the ice was very thin and soft, ice samples were collected by cutting blocks of ice using a stainless steel saw and putting them quickly into plastic containers to minimize brine drainage. Later the same day, the ice blocks were melted at room temperature [cf. *Rintala et al*., 2014], and the melted samples were prepared for particle (a_p) and CDOM (a_{CDOM}) absorption measurements. The samples were measured in bulk, so no vertical variation is resolved. For measurement of CDOM absorption, 0.2 μm membrane filters (Pall Acrodisk PF with Supor membrane) and precleaned all-plastic syringes were used. The samples were filtered into precombusted amber glass vials, and stored at 4°C until the absorbance was measured using a Shimadzu UV-1800 spectrophotometer. A 10 cm quartz cuvette with pure water as reference was used, and absorbance values were converted to absorption coefficients for the wavelength range 280–700 nm. For wavelengths longer than 700 nm CDOM absorption was assumed to be zero.

For measurement of particle absorption, the meltwater was filtered through Whatman GF/F ∅25 mm glass fiber filters using low vacuum. The filters were placed in Petri dishes, wrapped in aluminum foil, and stored at −80°C until analysis. To determine the particle absorption coefficient a_p in the range 280–900 nm, the transmittance-reflectance (T-R) method [*Tassan and Ferrari*, 2002] was applied. This technique involves measuring the transmittance and reflectance of the filter in a spectrophotometer, alternating the side of the filter facing the light source. The four different spectra are subsequently used to calculate the absorption coefficient.

2.2. Model

A radiative transfer model based on DISORT [*Jin and Stamnes*, 1994; *Thomas and Stamnes*, 1999; *Stamnes et al*., 2011] called AccuRT [*Hamre et al*., 2014] (version 1.0.613, available from Geminor Inc., Maplewood, NJ, USA) was used to model the albedo and transmittance of the sea ice. AccuRT is a radiative transfer model for a plane-parallel, coupled atmosphere-snow–ice-ocean domain, which employs the discrete-ordinate method to solve the radiative transfer equation. AccuRT includes atmospheric gases, aerosols, clouds, and snow materials in an upper slab, which has refractive index equal to 1, as well as sea ice and water in a lower slab, which has a refractive index equal to that of ice or water. Further, each slab may have multiple layers with inherent optical properties (IOPs) that are constant within each layer, but may differ between

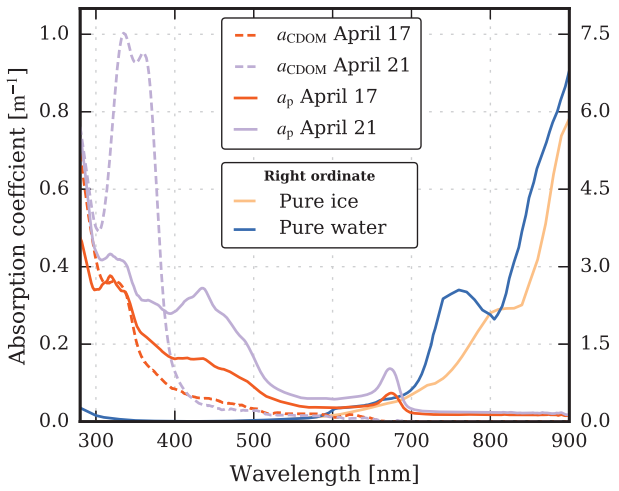

Figure 2. Measured spectral absorption by particles (a_p) and CDOM (a_{CDOM}) [values on the left ordinate axis]. Shown also are absorption coefficients for pure ice [*Warren and Brandt*, 2008] and pure water [*Pope and Fry*, 1997; *Segelstein*, 1981] (values on the right ordinate axis). These spectra were used as inputs to the AccuRT simulations. Particle and CDOM samples were collected only on 17 and 21 April.

adjacent layers. Since the refractive index of ice is close to that of water [*Warren and Brandt*, 2008; *Pope and Fry*, 1997; *Segelstein*, 1981], a fair approximation is to keep the refractive index constant with depth in the lower slab, also when this slab includes an ice layer above the water layer. Snow on top of the ice in the upper slab and ice inclusions (brine pockets, air bubbles, and impurities) are represented as spherical particles with a given size distribution and refractive index, and Mie theory, or a parameterized version of it, is used to calculate the IOPs. For this study the parameterized version is used, since it is accurate enough for the wavelength range considered [*Stamnes et al.*, 2011]. This version uses the Henyey-Greenstein phase function, but calculates the asymmetry parameter g based on the radius and refractive index of the spheres.

Biogenic or terrigenous particulates may be included in the ice by specifying the imaginary part m_i of the particulates' refractive index. It is related to the absorption coefficient a of the particulates, which are assumed to be evenly distributed throughout the ice slab. Thus

$$m_i = \frac{a}{\phi_{\text{imp}}} \frac{\lambda}{4\pi}, \tag{1}$$

where λ is the wavelength and ϕ_{imp} is the volume fraction occupied by impurity particles. The factor $1/\phi_{\text{imp}}$ is needed to convert the absorption coefficient of distributed particles (Figure 2) to that of the bulk material comprising the particles.

3. Results

3.1. Measurements

Figure 2 shows measured absorption coefficients for particulate and dissolved constituents in the ice. Each day, two ice samples were collected for melting and consequent filtering for measurement of particulate and dissolved absorption coefficients. Figure 2 shows the mean of the measured values for the two samples. On 17 April, the difference between the CDOM absorption coefficients obtained from the two samples (not shown) was found to be small in the visible range, but to reach 0.4 m^{-1} around 280 nm. On 21 April, the greatest difference between the CDOM absorption coefficients obtained from the two samples (also not shown) was found to be in the range 300–400 nm, where it reached 0.6 m^{-1} at the most, highlighting high spatial variability. Figure 2 shows that for wavelengths longer than 400 nm, particles contribute more to the total absorption than CDOM, while for wavelengths shorter than 400 nm CDOM gave the most significant contribution to the total absorption on 21 April.

Figure 3 shows the mean values of measured albedo and transmittance. Because the ice was fairly homogeneous, the variation along the transect was small, as indicated in Figure 3 by the narrow shaded area around each line that represents the ± 1 standard deviation from the mean values. On 21 April the first three positions and the last position (closest to the entrance hole) were disregarded in Figure 3, since the transmittance values at these positions were notably lower than at the other positions. Inclusion of those four transmittance values would lead to (wavelength dependent) standard deviations for transmittance that were 2–6 times larger than those presented in Figure 3b. The area farthest away from the entrance hole may have been subject to rafting of ice, creating a patch of thicker ice, and the position

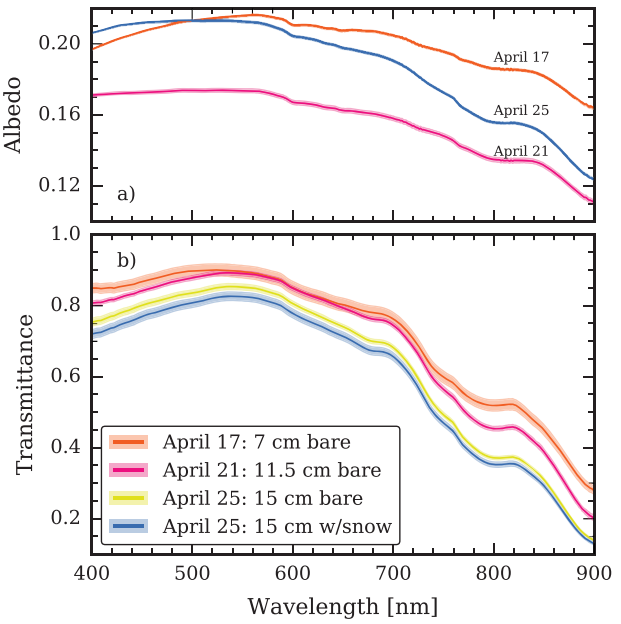

Figure 3. Measured (a) albedo and (b) transmittance for the 3 days. The shaded area around each line represents the ±1 standard deviation for all measurements along the transect. The number of spectra was 42, 17, 11, and 14 for 17 April, 21 April, 25 April (bare ice), and 25 April (2 mm snow cover on ice), respectively.

closest to the entrance hole may have been influenced by slush from the creation of the hole, air bubbles being pushed under the ice by the sled, or shading by the operator. The exact cause of these four low transmittance values is, however, not clear.

The transmittance generally becomes lower as the ice becomes thicker, but on 17 and 21 April the values in Figure 3b are seen to be almost equal in the region 550–650 nm (cf. section 4.1). The thin snow cover on 25 April caused a small decrease (less than 8%) in transmittance compared to that for bare ice on the same day. The albedo (Figure 3a) was lowest on 21 April, and highest on 17 April, except for wavelengths shorter than 500 nm, where higher values occurred on 25 April. Unlike the transmittance, which was measured along a transect, the albedo was measured at a fixed location. Therefore, the variances of the measured albedo was small compared to that of transmittance. The standard deviations did not exceed 0.0015 any day or wavelength. Table 1 summarizes bulk values of albedo α and transmittance T, given as

$$\alpha_{\text{bulk}} = \frac{\int \alpha(\lambda) F_s(\lambda)\, d\lambda}{\int F_s(\lambda)\, d\lambda}; \quad T_{\text{bulk}} = \frac{\int T(\lambda) F_s(\lambda)\, d\lambda}{\int F_s(\lambda)\, d\lambda}, \tag{2}$$

where F_s is the incoming solar irradiance, and λ is wavelength. The integration interval is either 400–900 nm or 400–700 nm (PAR), as indicated in Table 1.

3.2. Simulations

In the radiative transfer simulations by means of AccuRT, both the resolution and the bandwidth were set to 1 nm, and the simulated albedo and transmittance spectra were postprocessed with a Gaussian smoothing filter (standard deviation 5 nm). The parameters used in the simulations are given in Table 2. Sea ice was represented using a single, uniform layer.

Figure 4 shows the difference between simulated values and the observed mean values in Figure 3. For most wavelengths the absolute value of the difference in Figure 4 is less than 5%, both for the transmittance and the albedo. For wavelengths shorter than about 600 nm the transmittance difference is negative, indicating that the simulated transmittance values are lower than the measured values, while for wavelengths longer than 650 nm the difference is mostly positive. The difference between simulated and

Table 1. Integrated Values of Measured Albedo and Transmittance (Equation (2))[a]

	17 Apr	21 Apr	25 Apr	25 Apr (Clean)
Ice thickness	7 cm	11.5 cm	14.6 cm	14.6 cm
Albedo[b]	0.20	0.16	0.19	
Albedo (PAR)	0.21	0.17	0.21	
Transmittance[b]	0.76	0.75	0.65	0.67
Transmittance (PAR)	0.86	0.84	0.77	0.80

[a]25 April (clean) refers to values obtained after removal of a thin layer of snow. As the snow was not removed under the albedo rack, the values there are left out.
[b]For the range 400–900 nm.

Table 2. Parameters Used as Inputs to AccuRT to Simulate Sea Ice Albedo and Transmittance on 17, 21, and 25 April With Snow Cover, and 25 April With Bare Ice (Clean)

	Value			
Quantity	17 Apr	21 Apr	25 Apr	25 Apr (Clean)
Solar zenith angle (°)	69.3	68.3	66.4	66.9
Cloud height (km)		6–8		
Cloud volume fraction (%)	0.0	10^{-6}	0.0	0.0
Snow thickness (cm)	0.0	0.0	0.1	0.0
Snow effective grain size (cm)			2.0	
Snow density (kg m^{-3})			200.0	
Ice thickness (cm)	7.0	11.5	14.6	14.6
Air bubbles volume fraction (%)	0.6	0.5	0.1	0.1
Air bubbles effective radius (mm)	0.40	0.40	0.40	0.40
Brine pockets volume fraction (%)	40.0	40.0	40.0	40.0
Brine pockets effective radius (mm)	1.0	1.0	1.0	1.0
Impurities volume fraction (%)	10^{-5}	10^{-5}	10^{-5}	10^{-5}
Absorption by impurities	See Figure 2	See Figure 2	Same as 21 April	

observed albedo values in Figure 4 is mostly negative for 17 April. For 21 April the difference is positive for wavelengths shorter than about 680 nm and negative for longer wavelengths, and for 25 April the difference is small but mostly negative. The difference between simulated and observed values is of the same magnitude for the albedo and the transmittance. The root mean square error for all wavelengths and measurement days is below 0.04 for the transmittance and below 0.02 for the albedo.

Figure 5 demonstrates the influence of various sea ice constituents on the simulations for 21 April. We see that the addition of only 0.5% bubbles to pure bulk ice has a significant effect on the entire transmittance or albedo spectrum, reducing the former and increasing the latter. The addition of brine pockets to the sea ice is seen to have a slightly different effect. While it also reduces the transmittance and increases the albedo at all wavelengths, the added water content gives a relatively higher absorption around 750 nm due to the difference between the absorption coefficients of pure ice and pure water (cf. Figure 2), which makes the transmittance spectrum steeper between 700 and 750 nm.

As could be expected from Figure 2, Figure 5 shows that the effect of adding impurities is strongest at the shortest wavelengths, where both the transmittance and the albedo are reduced by up to 10%. Adding a layer representing the light blue sled used to hold the under-ice radiometer led to an artificial increase of the transmittance, particularly for wavelengths shorter than about 740 nm, and a general artificial increase of albedo (though the albedo increase would not have been observed with the setup used here).

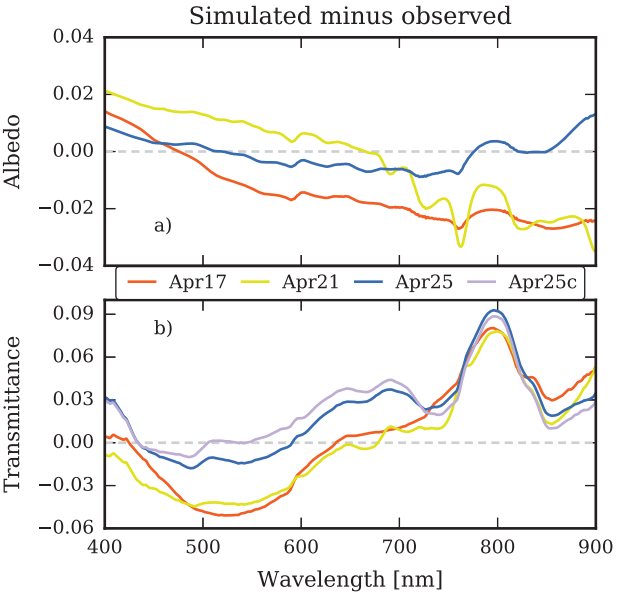

Figure 4. Difference between simulated and observed spectral values for (a) albedo and (b) transmittance, using parameters in Table 2 as inputs to AccuRT. As the snow was not removed under the albedo rack, Figure 4b does not have a curve for that case.

The inputs to AccuRT used to obtain the simulated results correspond to a very high amount of brine pockets in the ice (40%) and a low amount of air bubbles (0.6% or less). The surface temperature of the ice on 21 April was −5.8°C, and the seawater temperature was −1.6°C. If one assumes a linear temperature gradient, the mean temperature of the ice would be −3.7°C, which for the measured bulk ice salinity of 10 psu gives a brine volume of 13.4% following *Cox and Weeks* [1983]. Because some brine is likely to drain when ice samples are extracted [*Notz et al.*, 2005], 13.4% is probably a low

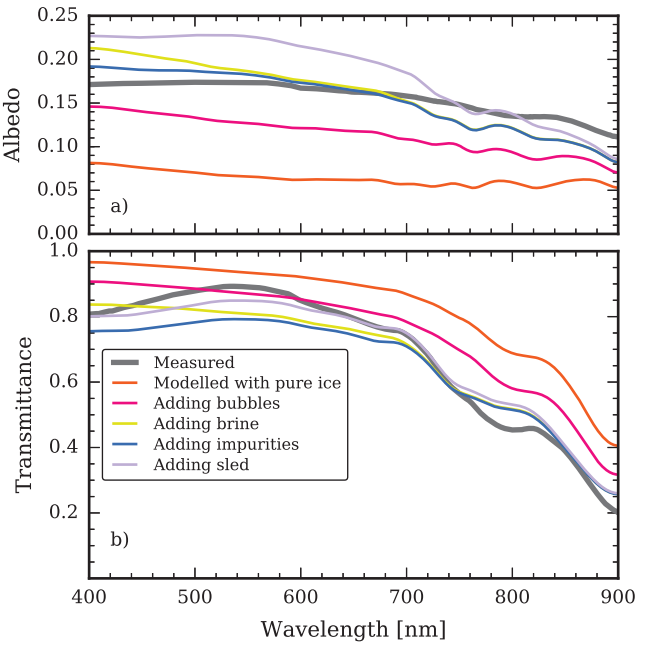

Figure 5. Sensitivity of (a) albedo and (b) transmittance, to different sea ice constituents on 21 April. The addition of inherent optical properties (IOPs) for different constituents as inputs to the AccuRT simulation is cumulative. Thus, the result labeled "simulation with pure ice," implies the use of IOPs for pure ice only; the result labeled "adding bubbles," implies the use of IOPs for pure ice and bubbles; the result labeled "adding brine," implies the use of IOPs for pure ice, bubbles, and brines; the result labeled "adding impurities," implies the use of IOPs for pure ice, bubbles, brines, and impurities; and the result labeled "adding sled," implies the use of IOPs for pure ice, bubbles, brines, impurities, and sled.

estimate for the brine volume, and the actual bulk salinity is likely higher than the measured value. When ice samples were extracted for filtering, the ice was observed to be very porous, supporting a high brine volume percentage. Visually, the ice appeared to have a vertically oriented structure with brine channels rather than pockets, which could make drainage more effective. The difference between the model-inferred and calculated values still seems rather large, and is discussed further in section 4.2.

4. Discussion

4.1. Measurements

Figure 2 shows that the absorption by CDOM between 300 and 400 nm is very high on 21 April, with two distinct peaks centered around 335 and 361 nm. The same tendency is seen also on 17 April, but with much lower peak values, and the largest peak at a slightly different wavelength. These peaks may indicate the presence of mycosporine-like amino acids (MAAs) in the ice. Similar absorption peaks were observed in ice-free Kongsfjorden later the same year by *Pavlov et al*. [2014], who attributed them to MAAs. The large difference in absorption between the two samples collected on 21 April indicates that the concentration of MAAs may have varied significantly over short distances. During the same period, the absorption by particles increased from 17 to 21 April, with distinct spectral peaks around 434 and 672 nm, indicative of buildup of biomass in the sea ice. Also, minor peaks around 318 nm are present in the a_p spectra. In surface ice layers of Baltic sea ice that were exposed to high irradiance levels, similar absorption peaks were observed in samples with a high ratio of MAA to chlorophyll [*Uusikivi et al*., 2010]. Thus, highly transparent thin ice may result in high light exposure levels that could result in MAA production by organisms in the ice, leading to a significant attenuation of ultraviolet radiation [cf. *Uusikivi et al*., 2010; *Piiparinen et al*., 2015].

Figure 3b shows that in parts of the spectrum the transmittance through 11.5 cm thick ice on 21 April was nearly equal to that through 7 cm thick ice on 17 April. As the ice on 21 April was both thicker and had stronger absorption by particles and CDOM (Figure 2), this may seem strange, but may be due differences between the 2 days in the direction of the incident light. On 17 April there were no clouds, implying that the incident light was mostly direct light from the sun, which was low in the sky with a solar zenith angle of about 69° (Table 2). Light scattering in clouds present on 21 April would cause a larger fraction of the light to hit the surface with a smaller angle of incidence, leading to less specular reflection and shorter traveling distances through the ice slab. Two simulations with AccuRT for the range 400–900 nm (not shown), one with clouds, one without, confirm this behavior, the former having 0.06–0.11 higher transmittance through a thin layer of ice.

Another curious feature observed in Figure 3 is that the sum of albedo and transmittance exceeds 1 at certain wavelengths in the visible range, with a maximum of 1.12 at 529 nm on 17 April. This may be partially caused by spatial variability of the ice, as incident and reflected irradiance was not measured at exactly the same location as the transmitted. Any variations in the ice over short distances would have an effect, and the ice where albedo was measured may have been disturbed by bending under the weight of the

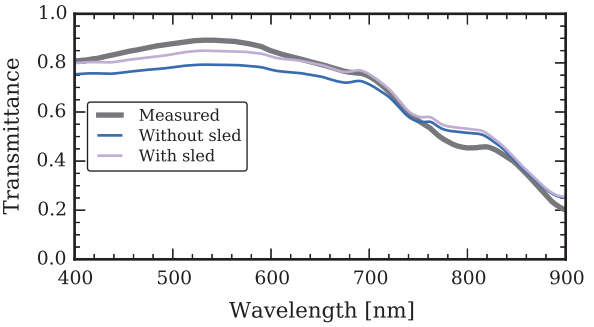

Figure 6. Simulated transmittance with and without sled, and measured transmittance, results from 21 April.

observers who set up the instruments. Furthermore, Figure 1 shows that the polystyrene sled used to hold the radiometer below the ice reflects light. Some of this reflected light is being scattered down again from the bottom surface of the ice, thus causing an artificial increase of transmittance that may be as large as 7% (see Figure 6).

4.2. Simulations

On the cloudy day of 21 April, two interesting local maxima appear in the spectral transmittance at 687 and 760 nm (Figure 5). These maxima are located in bands where atmospheric molecular oxygen absorbs significantly [*Greenblatt et al*., 1990], and could be explained as follows. Below the cloud layer, photons are traveling toward the ground with a wide distribution of directions. However, due to absorption, the amount of light reaching the ground decreases exponentially with traveling distance, so that vertically directed light will be least absorbed. Also, vertically directed light will have the lowest specular reflection from the ice and the least attenuation due to absorption passing through the ice, and hence the highest transmittance. For wavelengths with high atmospheric absorption, such as in oxygen absorption bands, the light incident on the surface will be more vertically oriented as a larger fraction of the oblique light is absorbed. Thus, the transmittance is higher in these bands. On cloud-free days, most of the light reaching the ground is contained in the solar beam, and there is no increased transmittance at wavelengths in absorption bands compared to that at other wavelengths. AccuRT simulations of light distributions at the ground (not shown) in the presence of clouds confirm the tendency of an enhanced fraction of vertically directed light in atmospheric absorption bands.

The fact that the two transmittance maxima are less evident in the measured spectra in Figure 5 likely indicates that the model overestimates this effect. Also, the dip in the simulated albedo seen at 760 nm (Figure 5a) is likely to be caused by vertically directed light in the oxygen absorption band, resulting in higher penetration of radiation into the ice and reduced albedo.

That the brine volume used in the model is more than 3 times that calculated from bulk salinity and temperature warrants commenting. The discrepancy seems unlikely to be caused wholly by brine drainage during ice sampling. As mentioned in section 4.4 halving the brine volume and increasing the effective radius of brine or air bubbles does not significantly impact the transmittance for wavelengths shorter than 700 nm. It is therefore possible that the need for such a high brine volume in the model could be connected to the same problem that causes the large difference seen around 800 nm (cf. section 4.3).

4.3. Model Uncertainties

The simulated results are reasonably good, but contain some uncertainties that are discussed below. Incident irradiance was not always accurately represented when clouds were present, partly due to difficulties finding a suitable set of parameters for the cloud layer. Further, a plane-parallel model cannot capture three-dimensional effects. For example, on 25 April there were scattered clouds not covering the sun, which could lead to irradiance levels above those under clear sky, due to additional light scattered from the clouds. This three-dimensional effect would also lead to a change in the average direction of the incoming solar radiation, which, as discussed above, could influence both the transmittance and the albedo.

Snow is represented in the model by spherical ice particles with a given effective radius. This representation is not realistic for the thin slushy snow with connected snow grains, present on 25 April. Therefore, the definition of the snow layer in the simulations is the result of an effort to tune the model to the observations, rather than accurately representing the actual conditions. The layer thickness was set to 1 mm, and the effective radius of the snow grains was much larger than the thickness of the snow layer (Table 2). Although unrealistic, it gave reasonable values for albedo and transmittance.

For the ice there are uncertainties with respect to measurement of impurity absorption coefficients, particularly in the visible region where organic materials are strong absorbers, making it harder to simulate

ultraviolet and visible irradiances than irradiances in the near-infrared region. Furthermore, ice samples were not taken on 25 April, so impurity absorption spectra for that day were assumed to be the same as those on 21 April, which may be a significant source of error in the shorter end of the wavelength range considered here. The wavelength-independent scattering coefficient of the sled below the ice was based on a qualified guess intended to make the transmittance in the visible region close to the measured values. No optical measurements were made on the sled material, and one may speculate whether misrepresentation of the IOPs of the sled could explain the difference in the spectral slope seen between the measured and simulated spectrum from 400 nm to about 550 nm.

The fact that the ice is represented as a single layer could also make it harder to represent both albedo and transmittance at the same time. A single-layer approach was chosen to reduce the complexity of the modeling, and due to the fact that the ice was thin, and no information about the vertical structure of the ice was available. As such, more layers would introduce more unknowns, opening up to overfitting the results.

However, the uncertainties described above cannot explain the difference between simulated and measured transmittance values seen around 800 nm. It is unclear why our model is unable to simulate the measured transmittance in this spectral region. One possibility could be that it is the measurements that are erroneous, but other measurements have shown a similar spectral shape of the transmittance, with a weak minimum at around 790 nm. For example, *Rasmus et al*. [2002] and *Ehn et al*. [2004], who measured transmittance in the Gulf of Finland, through ice between 10 and 30 cm thick. The shape of the transmittance spectra around 800 nm in these two studies are similar to that for the measurements presented here. It should also be noted that the water in this region is brackish, having much lower salinities than the water in Kongsfjorden. Another example is *Frey et al*. [2011], who observed a similar spectral shape around 800 nm for 0.83 m thick ponded ice. Since we are unable to simulate the observed behavior of the transmittance in this spectral region, which has little influence from impurities, we are led to believe that there may be features in the IOPs of pure sea ice or brine pockets that we have not been able to account for in our model.

Our absorption model is based on tabulated values for the absorption coefficients of pure ice (a_i) and water (a_w). If the fresh ice is not fully formed, it may contain more liquid water than included in the brine pockets. A simple way of accounting for the changes in absorption relative to that for pure ice might be to use a linear combination of a_i and a_w as absorption coefficient, instead of a_i. However, as a_i and a_w are nearly equal at λ=800 nm (Figure 2), such an experiment does not yield much improvement in the simulated transmittance at this wavelength. Figure 7a shows the modifications (up to 80%) of the absorption coefficient of pure ice ("artificial a_i" in the figure) needed to reproduce the measured transmittance (Figure 7b) on 21 April, in the region around 800 nm.

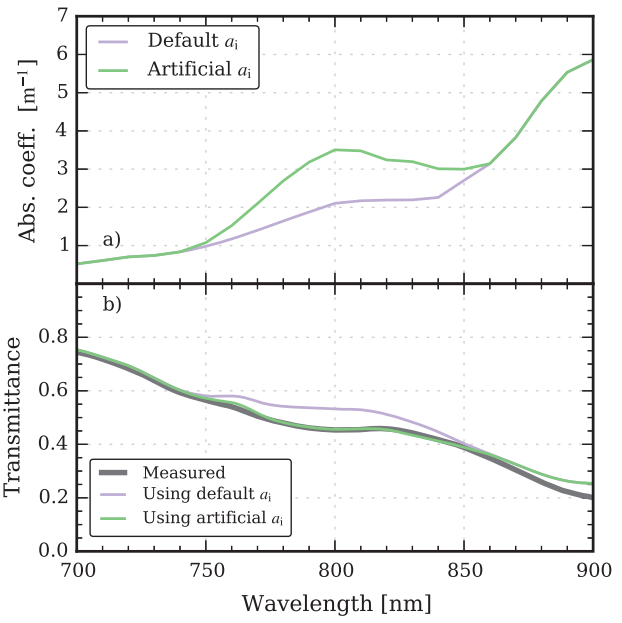

Figure 7. (a) Default and artificial absorption coefficient for ice. (b) Transmittance with the ice absorption coefficients from Figure 7a, along with measured values, for the case of 21 April.

Another hypothesis that might be used to account for the unexplained difference relates to temperature dependence of absorption coefficients. There is no temperature dependence in our absorption model, but for both pure ice [*Grundy and Schmitt*, 1998; *Grenfell*, 1983] and water [*Langford et al*., 2001] the absorption coefficient a has some dependence on temperature T. The simulated transmittance would have been different if the tabulated coefficients were obtained on ice or water with significantly different temperature than that of our in situ measurements. For water (see Figure 2), the model

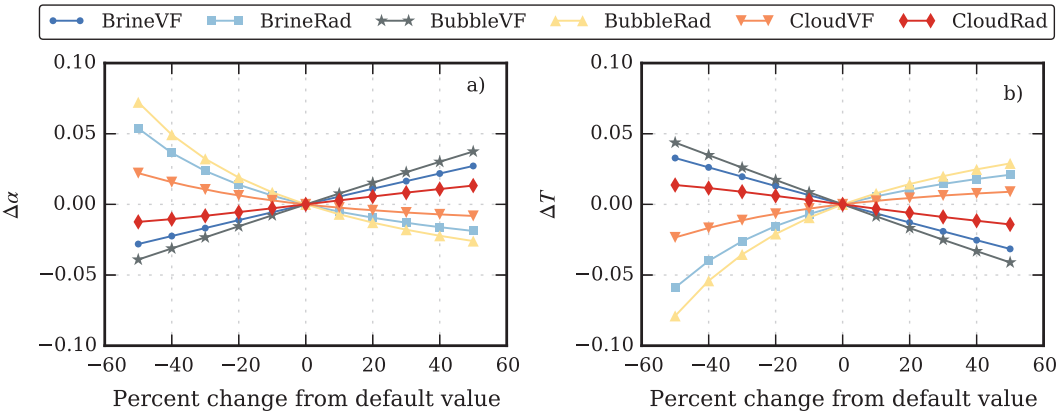

Figure 8. Change of (a) integrated albedo ($\Delta\alpha$) and (b) transmittance (ΔT) for a relative change of several model parameters. Default values are as given in Table 2 for 21 April. "VF" indicates volume fraction, and "Rad" indicates effective radius.

uses values from *Segelstein* [1981] or *Smith and Baker* [1981] in the near-infrared spectral range, the former of which were based on a water temperature of 25°C. *Langford et al.* [2001] reported values for da/dT in the spectral region 550–900 nm, for temperatures in the range 15–60°C. The values are in the range -0.007 $m^{-1}\,K^{-1}$ at 898 nm to $0.016\,m^{-1}\,K^{-1}$ at 738 nm. If one assumes that a similar gradient is valid down to around -2°C and that the water in Ny-Ålesund was at freezing temperature, the change in the absorption coefficient would be 8% at the most, and about 3% at 800 nm. Thus, a temperature dependent change in the absorption coefficient appears to be much smaller than 80% needed to account for the difference in transmittance.

For ice, the absorption model is based on values from *Warren and Brandt* [2008] which pertain to a nominal temperature of 266 K. In this region, *Warren and Brandt* [2008] use values due to *Grenfell and Perovich* [1981]. A more recent compilation by *Iwabuchi and Yang* [2011] provides values for the temperature range -113.5 to -3.15°C, based in part on *Warren and Brandt* [2008], showing no variation with temperature in the range of wavelengths considered here, making temperature dependence an unlikely cause of the mismatch also in this case.

Absorption coefficients also depend to some degree on salinity, but the effects are small [*Röttgers et al.*, 2014]. Furthermore, considering that the light travels mostly through ice, which is less saline, and that a similar spectral shape was seen by *Rasmus et al.* [2002] in waters with a salinity of only 2.8 psu, salinity does not appear to be a plausible explanation.

There is also a possibility that the scattering by brine pockets in this wavelength region is not accurately represented by the parameterized Mie code used, leading to incorrect transmittance. An indication that brine pockets are causing the problem can be seen in Figure 5. The curves for simulations with pure ice, and pure ice with air bubbles, both have a local minimum near 800 nm, while after the addition of brine pockets this is no longer seen.

4.4. Sensitivity to Model Parameters

To investigate the sensitivity of the albedo and the transmittance to changes in the main model parameters, we made a series of simulations in which each parameter was changed between -50% and $+50\%$ relative to its default value in Table 2. Figure 8 shows the resulting changes in integrated (equation (2)) PAR albedo and transmittance. For brine pockets and air bubbles, we see that an increase of the volume fraction has the opposite effect of an increase of the radius and that the integrated albedo and transmittance are more sensitive to a change in air bubbles than to a change in brine pocket inclusions. Changes in the volume fraction of cloud particles have the smallest effect.

We also see that the variations in integrated albedo and transmittance are of the same order when each parameter is varied, making it hard to find proper parameter values if only integrated radiometric quantities without spectral information are available. For example, the same integrated transmittance could be achieved with half the amount of brine if the bubble or brine radius is decreased concurrently. On

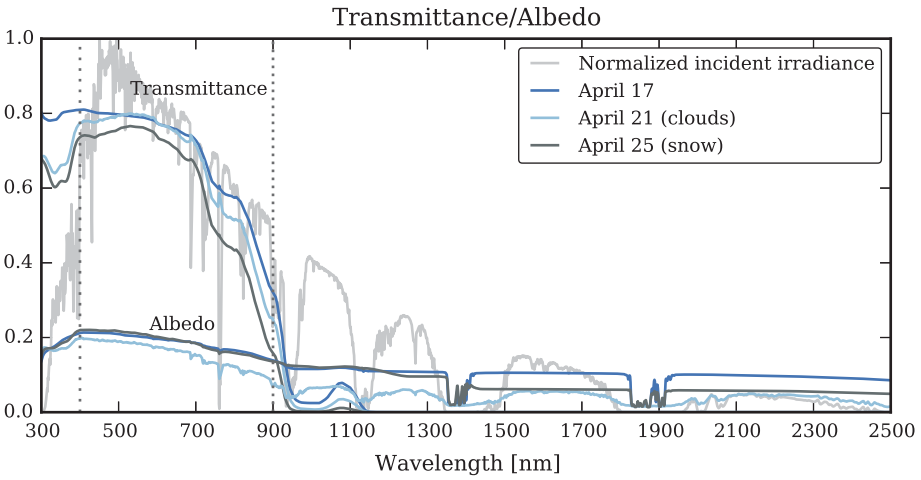

Figure 9. Simulated albedo and transmittance inferred from measured thin sea ice properties on 17, 21, and 25 April, together with the incoming normalized simulated irradiance spectrum at the ice surface. The wavelength range is 300–2500 nm, and dotted vertical lines indicate 400 and 900 nm, which are the limits of the spectral region for measured spectra. The noisy suppression in albedo seen around 1400 and 1900 nm is a numerical artifact caused by very low incoming irradiance due to strong water vapor absorption in the atmosphere.

performing such a simulation (not shown), we see that while there is very little change in transmittance for the shorter wavelengths, the simulated values deviate more from the measured values in the region 700–800 nm especially, as the reduced amount of water makes the slope of the spectrum flatter (cf. discussion of Figure 5 in section 3.2).

We see that the absolute changes for albedo and transmittance are of similar magnitude, meaning that the relative changes are greater for albedo, due to the lower initial values.

4.5. Extended Spectral Region

Figure 9 shows simulated albedo and transmittance for the range 300–2500 nm, along with a normalized version of one of the incident irradiance spectra. These simulations were performed to examine the total effect that this thin ice has on the broadband solar energy budget; to that end, the layer representing the IOPs of the measurement sled was not included. The transmittance is essentially zero for the wavelengths longer than about 1150 nm, falling off from the peak at 1070 nm to values around 10^{-11} at 1350 nm. The albedo on the other hand has nonzero values also in the near-infrared range due to specular reflection from the ice surface. Both cases without clouds show very little variability, except for two ranges, 1340–1430 nm and 1810–1910 nm, where the albedo drops suddenly, and varies a lot. In these two ranges the incident irradiance is close to zero due to high water vapor absorption in the atmosphere, and numerical difficulties occurred in the computation of the specular surface reflection.

The albedo is highest in the near-infrared for the case with bare ice and clear sky on 17 April, mainly due to high specular surface reflection when there are no clouds or snow that may redistribute the solar beam coming in at a near grazing angle of incidence to make the average propagation direction more vertical. At large solar zenith angles, adding a very thin snow layer on bare ice causes a reduction in the specularly reflected irradiance that is greater than the increase it causes in upward irradiance scattered by the added snow grains; thus, it can actually reduce the albedo. A comparison of Figure 9 with a simulation for 25 April without snow (not shown) shows that snow covering the ice increased the albedo for wavelengths shorter than about 1350 nm, but reduced the albedo for wavelengths longer than about 1350 nm. It should be noted, however, that the spectrally integrated albedo defined in equation (2) increased for snow-covered ice. A reduction in the near-infrared albedo of snow-covered ice can be seen in Figure 9 for wavelengths longer than 1340 nm on the gray curve representing 25 April.

It is also interesting to note that clouds reduce the spectral albedo at all wavelengths, which again can be explained by the redistribution of the incident light, which for this low sun-scenario is toward the vertical direction.

On both 17 and 25 April, 17% of the total energy is reflected, while on 21 April the corresponding percentage was 14%. The percentage of transmitted energy was lowest on 25 April at 47%, with 53 and 54% on 17 and 21 April, respectively. The energy absorbed in the ice increases as the ice becomes thicker: 30% for a thickness of 7 cm, 32% for a thickness of 11.5 cm, and 35% for a thickness of 14.6 cm. Assuming for now that all the absorbed energy goes to melting of ice—though in reality it will rather slow down growth—this corresponds to melt rates of 1.2, 0.8, and 1.6 mm h^{-1}, for 17, 21, and 25 April, respectively. A simple formulation for thermodynamic sea ice growth is [*Leppäranta*, 1993] $dh/dt = Q/\rho_i L$, where h is ice thickness, $\rho_i = 917\,\mathrm{kg\,m^{-3}}$ is the ice density, and $L = 3.35\times10^5\,\mathrm{J\,kg^{-1}}$ is the latent heat of fusion. Q, the heat flux from ice to air, is given as $\kappa_i(T_w - T_{air})/(h + \kappa_i/\kappa_a)$, where $\kappa_i = 2\,\mathrm{W\,m^{-1}\,K^{-1}}$ is the heat conductivity of sea ice, κ_a is a heat transfer coefficient for air and $\kappa_i/\kappa_a \approx 0.1$ m, T_{air} is the air temperature, and T_w is the temperature at the ice-ocean interface. Using temperatures measured at the weather station in Ny-Ålesund near the times of the spectral observations as T_{air}, and $-1.6°$C as T_w, we get ice growth rates of 0.9, 1.0, and 0.5 mm h^{-1}, for 17, 21, and 25 April, respectively. These values are of similar scale to the melt rates due to absorption of solar radiation. The net effect of sum of growth and melt becomes -0.3, 0.2, and -1.1 mm h^{-1}, for 17, 21, and 25 April, respectively, while the observed growth between these days were 0.4–0.5 mm h^{-1}. While such simple estimates are not accurate, they do demonstrate that absorption of solar radiation in this ice can be a significant limiting factor to the sea ice growth.

5. Conclusion

This study is one of few that focus on radiative transfer in newly formed thin sea ice. Studies to further understanding of such new ice is of increasing importance in an Arctic Ocean where the ice cover becomes more seasonal, and possibly more dynamic, leading to more new ice. Improving our understanding on this area can help reduce uncertainties for the partitioning of solar radiation during spring and autumn, and hence the total energy budget of the Arctic.

We found 7–15 cm thick growing ice to be very soft, and to possibly contain up to 40% brine volume, but only 0.6% air volume. The presence of mycosporine-like amino acids in the ice appeared to have a significant spatial variability and day-to-day temporal variability, likely leading to a corresponding impact on the transmittance of ultra violet radiation. On average, the simulated albedo and transmittance of solar radiation were 0.16 and 0.51, respectively.

Under a cloudy sky we found molecular oxygen absorption bands in the atmosphere to favor light traveling less obliquely and thus slightly increase the fraction of light penetrating the ice within these bands compared to the penetration of light at wavelengths outside the bands. For large solar zenith angles, a cloud layer was found to increase the ice transmittance at all wavelengths, because it shifts the average direction of the light toward the vertical. Also, at large solar zenith angles, a thin layer of snow on top of the ice was found to increase albedo only for wavelengths shorter than about 1350 nm. For longer wavelengths, the albedo was found to decrease when a thin layer of snow was added. This decrease is due to reduction in specular reflection at the ice-snow interface, caused by the snow having scattered the incident light, such that it arrives from a smaller average zenith angle.

The plane-parallel model could reproduce measured spectral albedo and transmittance fairly well, with a transmittance deviation within 5% for most of the spectral region. We do see an unexplained deviation occurred in the vicinity of 800 nm, perhaps indicating the need for new laboratory measurements on pure ice, or improved modeling of brine pocket optical properties at these wavelengths. Still the model may be a useful tool for simulating a variety of thin ice cases.

Acknowledgments

We thank Pekka Kosloff and the staff at Sverdrup Station and Kings Bay in Ny Ålesund for their support with data collection. This study was supported by the Research Council of Norway through the projects "STASIS" (221961) and "AMORA" (193592), with additional support from the Centre for Ice Climate and Ecosystems (ICE) at the Norwegian Polar Institute. The AccuRT model is available for purchase from Geminor Inc. (sales@geminor.com). Measured irradiance and absorption coefficients are available from the authors on request (torbjorn.taskjelle@uib.no). We also thank Bonnie Light and Jens Ehn for thorough reviews that helped improve the manuscript.

References

Arrigo, K. R., G. van Dijken, and S. Pabi (2008), Impact of a shrinking Arctic ice cover on marine primary production, *Geophys. Res. Lett.*, *35*, L19603, doi:10.1029/2008GL035028.

Cox, G. F. N., and W. F. Weeks (1983), Equations for determining the gas and brine volumes in sea-ice samples, *J. Glaciol.*, *29*, 306–316.

Ehn, J., M. A. Granskog, A. Reinart, and A. Erm (2004), Optical properties of melting landfast sea ice and underlying seawater in Santala Bay, Gulf of Finland, *J. Geophys. Res.*, *109*, C09003, doi:10.1029/2003JC002042.

Ehn, J. K., B. J. Hwang, R. Galley, and D. G. Barber (2007), Investigations of newly formed sea ice in the Cape Bathurst polynya: 1. Structural, physical, and optical properties, *J. Geophys. Res.*, *112*, C05002, doi:10.1029/2006JC003702.

Ehn, J. K., C. J. Mundy, D. G. Barber, H. Hop, A. Rossnagel, and J. Stewart (2011), Impact of horizontal spreading on light propagation in melt pond covered seasonal sea ice in the Canadian Arctic, *J. Geophys. Res.*, *116*, C00G02, doi:10.1029/2010JC006908.
Eisen, O., and C. Kottmeier (2000), On the importance of leads in sea ice to the energy balance and ice formation in the Weddell Sea, *J. Geophys. Res.*, *105*, 14,045–14,060, doi:10.1029/2000JC900050.
Frey, K. E., D. K. Perovich, and B. Light (2011), The spatial distribution of solar radiation under a melting Arctic sea ice cover, *Geophys. Res. Lett.*, *38*, L22501, doi:10.1029/2011GL049421.
Gerland, S., and A. H. Renner (2007), Sea-ice mass-balance monitoring in an Arctic fjord, *Ann. Glaciol.*, *46*(1), 435–442, doi:10.3189/172756407782871215.
Gerland, S., J.-G. Winther, J. B. Ørbæk, and B. V. Ivanov (1999), Physical properties, spectral reflectance and thickness development of first year fast ice in Kongsfjorden, Svalbard, *Polar Res.*, *18*(2), 275–282, doi:10.1111/j.1751-8369.1999.tb00304.x.
Greenblatt, G. D., J. J. Orlando, J. B. Burkholder, and A. R. Ravishankara (1990), Absorption measurements of oxygen between 330 and 1140 nm, *J. Geophys. Res.*, *95*, 18,577–18,582, doi:10.1029/JD095iD11p18577.
Grenfell, T. C. (1979), The effects of ice thickness on the exchange of solar radiation over the polar oceans, *J. Glaciol.*, *22*, 305–320.
Grenfell, T. C. (1983), A theoretical model of the optical properties of sea ice in the visible and near infrared, *J. Geophys. Res.*, *88*, 9723–9735, doi:10.1029/JC088iC14p09723.
Grenfell, T. C., and G. A. Maykut (1977), The optical properties of ice and snow in the Arctic Basin, *J. Glaciol.*, *18*, 445–463.
Grenfell, T. C., and D. K. Perovich (1981), Radiation absorption coefficients of polycrystalline ice from 400–1400 nm, *J. Geophys. Res.*, *86*, 7447–7450, doi:10.1029/JC086iC08p07447.
Grundy, W. M., and B. Schmitt (1998), The temperature-dependent near-infrared absorption spectrum of hexagonal H_2O ice, *J. Geophys. Res.*, *103*, 25,809–25,822, doi:10.1029/98JE00738.
Hamre, B., J.-G. Winther, S. Gerland, J. J. Stamnes, and K. Stamnes (2004), Modeled and measured optical transmittance of snow-covered first-year sea ice in Kongsfjorden, Svalbard, *J. Geophys. Res.*, *109*, C10006, doi:10.1029/2003JC001926.
Hamre, B., S. Stamnes, J. J. Stamnes, and K. Stamnes (2014), AccuRT: A versatile tool for radiative transfer in coupled media like atmosphere-ocean systems, in *Ocean Optics XXII*, Portland, Maine. [Available at: http://www.geminor.com/media/Hamre_OO2014_A0_portrait_v3.pdf.]
Hudson, S. R., M. A. Granskog, A. Sundfjord, A. Randelhoff, A. H. H. Renner, and D. V. Divine (2013), Energy budget of first-year Arctic sea ice in advanced stages of melt, *Geophys. Res. Lett.*, *40*, 2679–2683, doi:10.1002/grl.50517.
Ishikawa, N., A. Takizawa, T. Kawamura, K. Shirasawa, and M. Leppäranta (2002), Changes in radiation properties and heat balance with sea ice growth in Saroma Lagoon and the Gulf of Finland, in *Ice in the Environment: Proceedings of the 16th IAHR International Symposium on Ice*, vol. 3, pp. 194–200, University of Otago, Dunedin, New Zealand.
Iwabuchi, H., and P. Yang (2011), Temperature dependence of ice optical constants: Implications for simulating the single-scattering properties of cold ice clouds, *J. Quant. Spectrosc. Radiat. Transfer*, *112*(15), 2520–2525, doi:10.1016/j.jqsrt.2011.06.017.
Jin, Z., and K. Stamnes (1994), Radiative transfer in nonuniformly refracting layered media: Atmosphere-ocean system, *Appl. Opt.*, *33*(3), 431–442, doi:10.1364/AO.33.000431.
Langford, V. S., A. J. McKinley, and T. I. Quickenden (2001), Temperature dependence of the visible-near-infrared absorption spectrum of liquid water, *J. Phys. Chem. A*, *105*(39), 8916–8921, doi:10.1021/jp010093m.
Leppäranta, M. (1993), A review of analytical models of sea-ice growth, *Atmos. Ocean*, *31*(1), 123–138, doi:10.1080/07055900.1993.9649465.
Light, B., T. C. Grenfell, and D. K. Perovich (2008), Transmission and absorption of solar radiation by Arctic sea ice during the melt season, *J. Geophys. Res.*, *113*, C03023, doi:10.1029/2006JC003977.
Light, B., D. K. Perovich, M. Webster, C. Polashenski, and R. Dadic (2015), Optical properties of melting first-year Arctic sea ice, *J. Geophys. Res. Oceans*, *120*, 7657–7675, doi:10.1002/2015JC011163.
Maslanik, J. A., C. Fowler, J. Stroeve, S. Drobot, J. Zwally, D. Yi, and W. Emery (2007), A younger, thinner Arctic ice cover: Increased potential for rapid, extensive sea-ice loss, *Geophys. Res. Lett.*, *34*, L24501, doi:10.1029/2007GL032043.
Nicolaus, M., S. Gerland, S. R. Hudson, S. Hanson, J. Haapala, and D. K. Perovich (2010), Seasonality of spectral albedo and transmittance as observed in the Arctic Transpolar Drift in 2007, *J. Geophys. Res.*, *115*, C11011, doi:10.1029/2009JC006074.
Nicolaus, M., C. Petrich, S. R. Hudson, and M. A. Granskog (2013), Variability of light transmission through Arctic land-fast sea ice during spring, *Cryosphere*, *7*(3), 977–986, doi:10.5194/tc-7-977-2013.
Nicolaus, M., C. Wang, S. Gerland, N. Li, Z. Li, B. Cheng, M. A. Granskog, L. Shi, R. Lei, Q. Li, and P. Lu (2015), Advancing the understanding of variations of Arctic sea ice optical and thermal behaviors through an international research and mobility project, *Adv. Polar Sci.*, *26*(2), 179–187, doi:10.13679/j.advps.2015.2.00179.
Notz, D., J. S. Wettlaufer, and M. G. Worster (2005), A non-destructive method for measuring the salinity and solid fraction of growing sea ice in situ, *J. Glaciol.*, *51*(172), 159–166, doi:10.3189/172756505781829548.
Pavlov, A. K., A. Silyakova, M. A. Granskog, R. G. Bellerby, A. Engel, K. G. Schulz, and C. P. Brussaard (2014), Marine CDOM accumulation during a coastal Arctic mesocosm experiment: No response to elevated pCO_2 levels, *J. Geophys. Res. Biogeosci.*, *119*, 1216–1230, doi:10.1002/2013JG002587.
Perovich, D. K. (1991), Seasonal changes in sea ice optical properties during fall freeze-up, *Cold Reg. Sci. Technol.*, *19*(3), 261–273, doi:10.1016/0165-232X(91)90041-E.
Perovich, D. K. (1996), The optical properties of sea ice, U. S. Cold Regions Research and Engineering Laboratory Monograph 96–1, 25 pp., Hanover, N. H.
Perovich, D. K., and T. C. Grenfell (1981), Laboratory studies of the optical-properties of Young Sea ice, *J. Glaciol.*, *27*(96), 331–346.
Piiparinen, J., S. Enberg, J.-M. Rintala, R. Sommaruga, M. Majaneva, R. Autio, and A. V. Vähätalo (2015), The contribution of mycosporine-like amino acids, chromophoric dissolved organic matter and particles to the UV protection of sea-ice organisms in the Baltic Sea, *Photochem. Photobiol. Sci.*, *14*(5), 1025–1038, doi:10.1039/C4PP00342J.
Pope, R. M., and E. S. Fry (1997), Absorption spectrum (380–700 nm) of pure water. II. Integrating cavity measurements, *Appl. Opt.*, *36*(33), 8710–8723, doi:10.1364/AO.36.008710.
Rasmus, K., J. K. Ehn, M. A. Granskog, E. Kärkäs, M. Leppäranta, A. Lindfors, A. Pelkonen, S. Rasmus, and A. Reinart (2002), Optical measurements of sea ice in the Gulf of Finland, *Nord. Hydrol.*, *33*(2–3), 207–226.
Rintala, J.-M., J. Piiparinen, J. Blomster, M. Majaneva, S. Müller, J. Uusikivi, and R. Autio (2014), Fast direct melting of brackish sea-ice samples results in biologically more accurate results than slow buffered melting, *Polar Biol.*, *37*(12), 1811–1822, doi:10.1007/s00300-014-1563-1.
Röttgers, R., D. McKee, and C. Utschig (2014), Temperature and salinity correction coefficients for light absorption by water in the visible to infrared spectral region, *Opt. Express*, *22*(21), 25,093–25,108, doi:10.1364/OE.22.025093.
Segelstein, D. J. (1981), The complex refractive index of water, MS thesis, Univ. of Mo., Kansas City, Mo.

Smith, R. C., and K. S. Baker (1981), Optical properties of the clearest natural waters (200–800 nm), *Appl. Opt.*, *20*(2), 177–184, doi:10.1364/AO.20.000177.

Stamnes, K., B. Hamre, J. J. Stamnes, G. Ryzhikov, M. Biryulina, R. Mahoney, B. Hauss, and A. Sei (2011), Modeling of radiation transport in coupled atmosphere-snow-ice-ocean systems, *J. Quant. Spectrosc. Radiat. Transfer*, *112*(4), 714–726, doi:10.1016/j.jqsrt.2010.06.006.

Tassan, S., and G. M. Ferrari (2002), A sensitivity analysis of the "transmittance–reflectance" method for measuring light absorption by aquatic particles, *J. Plankton Res.*, *24*(8), 757–774, doi:10.1093/plankt/24.8.757.

Thomas, G. E., and K. Stamnes (1999), *Radiative Transfer in the Atmosphere and Ocean*, Cambridge Univ. Press, Cambridge, U. K.

Uusikivi, J., A. V. Vähätalo, M. A. Granskog, and R. Sommaruga (2010), Contribution of mycosporine-like amino acids and colored dissolved and particulate matter to sea ice optical properties and ultraviolet attenuation, *Limnol. Oceanogr. Methods*, *55*(2), 703–713, doi:10.4319/lo.2010.55.2.0703.

Warren, S. G., and R. E. Brandt (2008), Optical constants of ice from the ultraviolet to the microwave: A revised compilation, *J. Geophys. Res.*, *113*, D14220, doi:10.1029/2007JD009744.

Zhang, X., and J. E. Walsh (2006), Toward a seasonally ice-covered Arctic Ocean: Scenarios from the IPCC AR4 model simulations, *J. Clim.*, *19*(9), 1730–1747, doi:10.1175/JCLI3767.1.